ADVANCED MATERIALS

www.advmat.de

An Ordered Ni_6-Ring Superstructure Enables a Highly Stable Sodium Oxide Cathode

Peng-Fei Wang, Mouyi Weng, Yao Xiao, Zongxiang Hu, Qinghao Li, Meng Li, Yi-Ding Wang, Xin Chen, Xinan Yang, Yuren Wen, Ya-Xia Yin, Xiqian Yu, Yinguo Xiao, Jiaxin Zheng, Li-Jun Wan, Feng Pan,* and Yu-Guo Guo**

Sodium-based layered oxides are among the leading cathode candidates for sodium-ion batteries, toward potential grid energy storage, having large specific capacity, good ionic conductivity, and feasible synthesis. Despite their excellent prospects, the performance of layered intercalation materials is affected by both a phase transition induced by the gliding of the transition metal slabs and air-exposure degradation within the Na layers. Here, this problem is significantly mitigated by selecting two ions with very different M—O bond energies to construct a highly ordered Ni_6-ring superstructure within the transition metal layers in a model compound ($NaNi_{2/3}Sb_{1/3}O_2$). By virtue of substitution of 1/3 nickel with antimony in $NaNiO_2$, the existence of these ordered Ni_6-rings with super-exchange interaction to form a symmetric atomic configuration and degenerate electronic orbital in layered oxides can not only largely enhance their air stability and thermal stability, but also increase the redox potential and simplify the phase-transition process during battery cycling. The findings reveal that the ordered Ni_6-ring superstructure is beneficial for constructing highly stable layered cathodes and calls for new paradigms for better design of layered materials.

Dr. P.-F. Wang, Dr. Y. Xiao, Dr. Y.-X. Yin, Prof. L.-J. Wan, Prof. Y.-G. Guo
CAS Key Laboratory of Molecular Nanostructure and Nanotechnology
CAS Research/Education Center for Excellence in Molecular Sciences
Beijing National Laboratory for Molecular Sciences (BNLMS)
Institute of Chemistry
Chinese Academy of Sciences (CAS)
Beijing 100190, P. R. China
E-mail: yxyin@iccas.ac.cn; ygguo@iccas.ac.cn

Dr. P.-F. Wang, Y.-D. Wang, Dr. Y.-X. Yin, Prof. L.-J. Wan, Prof. Y.-G. Guo
School of Chemical Sciences
University of Chinese Academy of Sciences
Beijing 100049, P. R. China

M. Weng, Z. Hu, M. Li, X. Chen, Prof. Y. Xiao, Prof. J. Zheng, Prof. F. Pan
School of Advanced Materials
Peking University
Shenzhen Graduate School
Shenzhen 518055, P. R. China
E-mail: panfeng@pkusz.edu.cn

Dr. Q. Li, Dr. X. Yang. Dr. Y. Wen, Prof. X. Yu
Beijing National Laboratory for Condensed Matter Physics
Institute of Physics
CAS
Beijing 100190, P. R. China

The ORCID identification number(s) for the author(s) of this article can be found under https://doi.org/10.1002/adma.201903483.

DOI: 10.1002/adma.201903483

Layered sodium transition-metal oxides Na_xMO_2 have been extensively investigated as the most promising cathode candidates in sodium-ion batteries (SIBs) because of their superior specific capacity and the simple analogies from the successful application of $LiMO_2$ in Li-ion battery systems.[1–8] In general, O3-type Na_xMO_2 (Na occupies octahedral sites) outperform their P2 analogs (Na occupies prismatic sites) in terms of the specific capacity due to the sufficient Na content.[9–11] However, two main challenges might hinder O3-type Na_xMO_2 cathodes from practical application. On one hand, most of O3-Na_xMO_2 compounds are very hygroscopic against moist atmosphere, leading to the formation of electrochemically inactive NaOH, $NaHCO_3$, or Na_2CO_3 by partial Na extraction. These alkaline species would accelerate the defluorination of polyvinylidene fluoride binder and corrosion of current collector due to their dissolution into *N*-methyl-2-pyrrolidone solvent, drastically impeding their practical viability.[12–16] On the other hand, extraction and insertion of Na ions from layered compounds inevitably leads to several first-order phase transformations sequences accompanied by multiple voltage plateaus and steps in the electrochemical curves,[17,18] incurring low diffusion coefficients and complicated cation diffusion mechanisms as additional energy barrier is needed in moving the Na ions from neighboring phase boundaries. So stepwise voltage profile and poor rate performance are often observed for O3-type cathodes because the asymmetries between the required multiple kinetic processes are inclined to impose an abrupt change in crystal structure and composition.[19]

Such poor structural stability with regard to multiple phase evolution has been found to be related to cationic ordering/disordering and the gliding of M oxide layers.[20,21] It is well established that three types of ordering exists in binary $Na_x[M1,M2]O_2$-layered oxides: cationic ordering, Na^+/vacancy ordering and charge ordering. Cationic ordering, related to the phase transition and structural stability, is commonly determined by the difference of M1 and M2 within transition metal layers. Large disparity in ionic radii and M—O bond energy tends to form ordered arrangement while small difference is favorable for

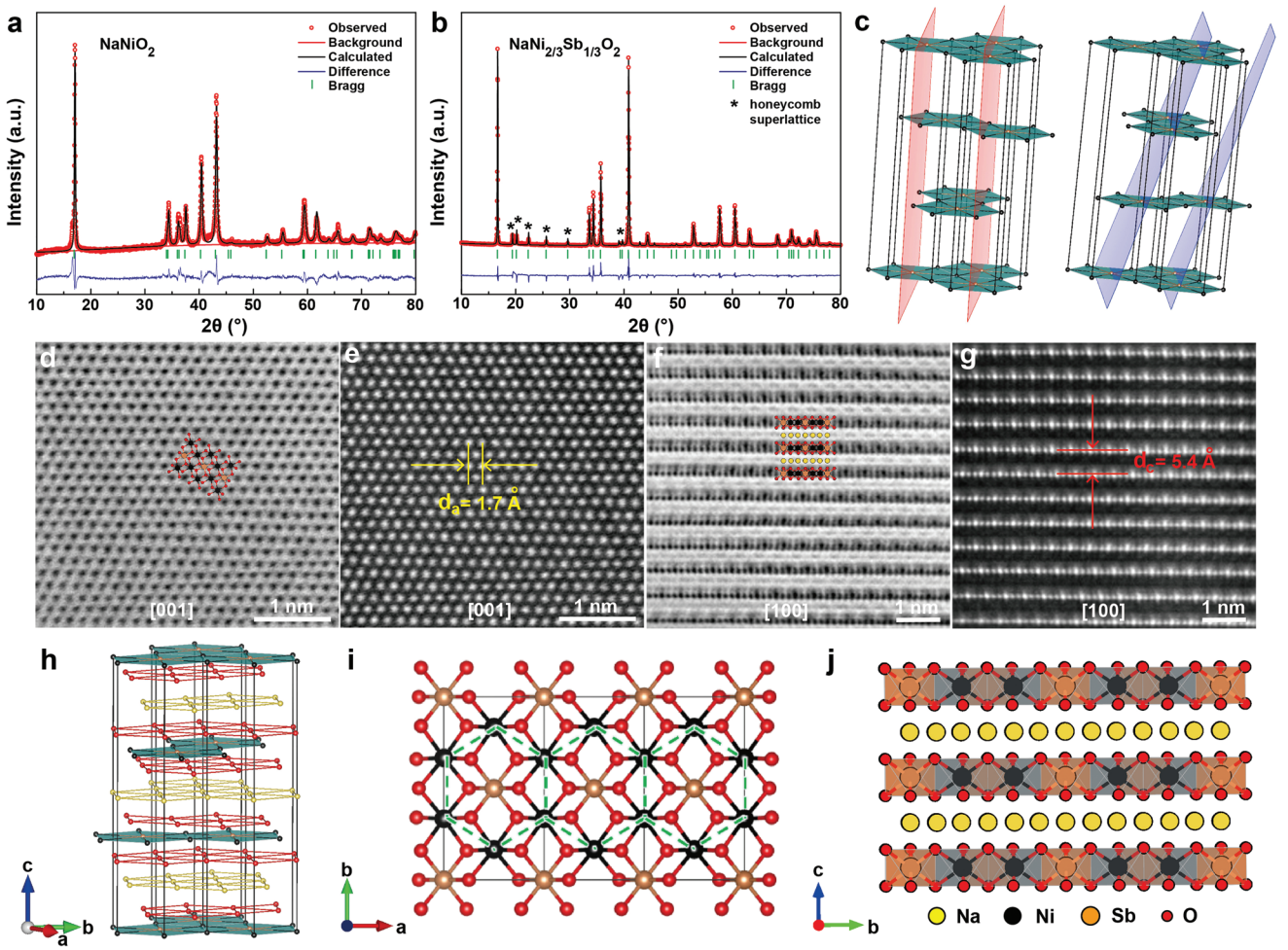

Figure 1. a,b) The XRD and Rietveld plots of $NaNiO_2$ (a) and $NaNi_{2/3}Sb_{1/3}O_2$ (b) samples. c) The (020) and (110) crystallographic planes of typical superlattice peaks. d) ABF and e) HAADF-STEM images of $NaNi_{2/3}Sb_{1/3}O_2$ at the [001] zone axis. f) ABF and g) HAADF-STEM image of $NaNi_{2/3}Sb_{1/3}O_2$ at the [100] zone axis. h–j) The crystal structure of $NaNi_{2/3}Sb_{1/3}O_2$ viewed along different directions.

forming disordered arrangement. Cationic ordering/disordering linked to complicated phase transformations and instable air exposure often accompanies stresses changes in structure and possible particles crack, which instead affect the shape of the voltage curve and cause battery performance degradation.[22–24] In this context, it is of great importance to tailor the structural stability to facilitate better material design. Of particular urgency is the study of cationic ordering tendencies between M chemistries and its driving force within the O3-type layered lattice structure.

Herein, for the first time, we present a combined experimental and theoretical study to elucidate the effects of intercalation cationic ordering on structural stability in layered O3 oxides using $NaNiO_2$ as a model system. By virtue of substitution of 1/3 nickel with antimony in $NaNiO_2$, a highly stabilized phase with honeycomb-type cationic ordered superlattice in the $Na[Ni_{2/3}Sb_{1/3}]O_2$ compound is established. The formed Ni_6-rings with super-exchange interaction by Ni/Sb ordering largely increases the air stability, thermal stability, and phase stability of pristine $NaNiO_2$. Moreover, sequential O3–P3–O1 phase transition process undergoes a symmetrical–asymmetrical–symmetrical electronic structural evolution during Na ions deintercalation/intercalation in $Na_{1-x}Ni_{2/3}Sb_{1/3}O_2$. And unique valence disproportionation is surprisingly detected in O1 phase supported by soft X-ray absorption spectra, magnetic moment, and radial distribution function. This study demonstrates the relationship between intercalating cationic ordering and structural stability in the O3 model structures, providing a firm platform to design high-stable and high-voltage cathodes for advanced SIBs.

The PXRD pattern of $NaNiO_2$ (**Figure 1**a) synthesized at 700 °C can be indexed to a monoclinic unit cell ($C2/m$, a = 5.3226(9) Å, b = 2.8501(1) Å, c = 5.5885(5) Å, and β = 110.448(4)°), suggesting a distorted O3-type structure owing to the a/b ratio (1.87) deviated from that of the ideal hexagonal system ($\sqrt{3} \approx 1.73$). The pattern of $NaNi_{2/3}Sb_{1/3}O_2$ (Figure 1b) were indexed to the monoclinic space group $C2/m$ (a = 5.3067(7) Å, b = 9.1879(2) Å, c = 5.6313(1) Å, and β = 108.246(1)°). The specific atomic positions and cell parameters are listed in Tables S1 and S2 (Supporting Information). Examination of the 2θ region between 17° and 30° reveals superlattice reflections based on the $C2/m$ model, as marked by asterisks in Figure 1b. In honeycomb $NaNi_{2/3}Sb_{1/3}O_2$ compounds, the 2:1 ordering of Ni/Sb

atoms in the *a*–*b* plane generates a unit cell larger by $\sqrt{3}a_0$ that yields superlattice reflections not described by the $R\bar{3}m$ α-$NaFeO_2$ subcell (where a_0 is basal plane cell parameter for α-$NaFeO_2$).[25] Reflections of typical superlattices at 2θ values of 19.1°, 19.9°, 22.1°, 25.3°, 29.3°, and 38.6° (Figure 1c and Figure S1, Supporting Information) are well indexed by corresponding crystallographic planes in this cell, indicative of a large degree of ordering within the layered structure. Density functional theory (DFT) calculations further demonstrate this honeycomb configuration has the lowest thermodynamic energy per formula unit (Figure S2, Supporting Information).

Detailed honeycomb-ordered structural information on $NaNi_{2/3}Sb_{1/3}O_2$ compounds was experimentally confirmed by atomic-scale aberration-corrected annular-bright field (ABF) and high-angle annular-dark-field (HAADF) scanning transmission electron microscopy (STEM). The positions of the Sb and Ni columns was marked by larger and smaller dark-dot contrast in the ABF-STEM images and bright-dot contrast in the HAADF-STEM images, respectively.[26] The light element Na and O columns in the layered structure are revealed by the faint dark-dot contrast with the interlayer positions in the ABF-STEM images. Ni/Sb atoms arrange in a hexagonal symmetry from the ABF-STEM images (Figure 1d) at the [001] zone axis. Corresponding HAADF-STEM images reveal the projected distance between the *M* atomic columns is 1.7 Å (Figure 1e). The dots of the O columns on both sides of the Ni/Sb layers demonstrate different darkness or sometimes vanish completely in the [100] ABF-STEM and HAADF-STEM images, which suggest some stacking faults as lateral displacements of the dot patterns in the $Ni_{2/3}Sb_{1/3}O_2$ layers (Figure 1f). The sequence Sb–Ni–Ni–Sb associated with the cationic honeycomb ordering in the TM layers is highlighted in HAADF-STEM images (Figure 1g) by the size change of the bright spots. Corresponding crystal structures of typical $NaNi_{2/3}Sb_{1/3}O_2$ with different perspectives are plotted in Figure 1h–j. Each SbO_6 octahedron is surrounded by six NiO_6 edge-sharing octahedra forming the Ni_6-ring honeycomb lattice. Ni_2SbO_6 layers and Na layers alternate with ABCABC oxygen stacking patterns. The Na^+ ions are intercalated within the Ni_2SbO_6 slabs and occupy an octahedral NaO_6 site.

To explore the effect of honeycomb superstructure on its structural stability, aging experiments (exposing materials to air for 10 days or soaking in water for 10 min followed by drying at 100 °C overnight) were performed. As shown in **Figure 2**a, the characteristic (111) peak of the O3-phase $NaNiO_2$ gradually weakens and vanishes during the air exposure process. In addition, a gradual shift of the (001) peak toward lower angles is observed as the formation of P3-type $Na_{1-x}H_xNiO_2$ upon exposure to air, originating from a migration of Na^+ ions out from the lattice to form impurities. Further IR spectra analysis shows the wavenumber located at 3636 and 868 cm^{-1} for the soaked sample can be assigned to the O—H and C—O bond vibration, respectively (Figure 2b). When $NaNiO_2$ samples are exposed to moist atmosphere, Na^+ ions are readily exchanged with H^+ ions by uptaking H_2O (Figure S3, Supporting Information) from atmosphere as the following process: $NaNiO_2 + xH_2O = Na_{1-x}H_xNiO_2 + x$NaOH, NaOH + CO_2 = $NaHCO_3$, 2NaOH + CO_2 = Na_2CO_3 + H_2O.[27,28] Even worse, the formed NaOH, $NaHCO_3$, and Na_2CO_3 are electrical insulators, which leads to the much decreased crystallinity (Figure S4, Supporting Information). In contrast, the X-ray diffraction (XRD) patterns of $NaNi_{2/3}Sb_{1/3}O_2$ are almost the identical with that of as-prepared sample upon exposing to air or soaking in water (Figure 2c). That is to say 1/3 Sb substitution obtains the Ni_6-ring superstructure, which is sufficient to endow $NaNi_{2/3}Sb_{1/3}O_2$ water-resistant to inhibit the spontaneous structure evolution and oxidation to higher valence state (Figure S5, Supporting Information).

In situ X-ray diffraction patterns during the heat treatment process were collected to better understand thermal stability of $NaNi_{2/3}Sb_{1/3}O_2$ (Figure 2d,e). The change of peak intensity and position of several main characteristic peaks located at 50°–65° and 66°–76.5° with a function of temperature are presented as 2D contour plots in Figure 2f,g. Note that the intensity of the superlattice peak characteristic of $NaNi_{2/3}Sb_{1/3}O_2$ centered at 17°–30° shows no obvious change, suggesting the honeycomb-ordered superstructure is very stable during the annealing treatment. Furthermore, all diffraction lines only show peak position shift without any shape change and no extra peaks beyond the O3 structure are detected. And an exact opposite evolution is clearly observed for the XRD pattern and the well-defined diffraction lines belonging to the monoclinic phase were completely recovered to the original positions upon cooling down to the room temperature, indicating superior thermal stability. Calculated total DFT energies (Figure 2h) demonstrate that ordered Ni_6-ring superstructure in $NaNi_{2/3}Sb_{1/3}O_2$ significantly enlarges the energy difference (4.356 vs 3.254 eV) between $Na_3Ni_2SbO_6$ and $Na_3Ni_2SbO_{5.5}$ when one atom was removed from the O3 structure, consequently breaking the M—O bond become more difficult, which could refrain the loss of crystal oxygen in the framework and promote higher structure stability over a wider temperature range.

By virtue of further DFT analysis, two characteristics in $NaNi_{2/3}Sb_{1/3}O_2$ are preferred to make its honeycomb structure more energy favorable. First, Ni_6-ring configuration has the minimum distorted Ni–O and Sb–O local octahedron. The specific bond length and bond angle of each octahedron in different configuration are listed in Tables S3–S13 (Supporting Information). This peculiarity in $NaNi_{2/3}Sb_{1/3}O_2$ guarantees a D_{3d} symmetry in electronic structure (Figures S6–S8), thus d_{xy} orbital degenerates with $d_{x2\text{-}y2}$ orbital and d_{xz} orbital degenerates with d_{yz} orbital in Ni atoms as shown in **Figure 3**a,b.[29] Second, Ni_6-ring configuration promises highly symmetric atomic structures within transition metal layers. The distance between neighboring Ni atoms in Jahn–Teller distorted $NaNiO_2$ is 2.860 Å (white dashed line) and 3.089 Å (yellow dashed line), respectively (Figure 3c). In $NaNi_{2/3}Sb_{1/3}O_2$, all neighboring Ni—Ni bonds indicate a length of 3.101 Å (Figure 3d), thus a high symmetry atomic structure within MO_2 slabs is established.

The two characteristics might originate from the elimination of magnetic frustration and the existence of a 90° Ni–O–Ni super-exchange interaction. When Sb replaces a Ni atom, every oxygen atom connects one Sb atom and two Ni atoms within MO_2 slabs. Considering Sb atom does not have any spin electrons, thus no magnetic frustration can be observed.[30] Similar with $LiNiO_2$,[31] $NaNiO_2$ can be considered as a prominent example of strong geometrically frustrated material as it shows neither spin nor orbital ordering, of which the frustration parameter value is estimated to be 1.8. However in

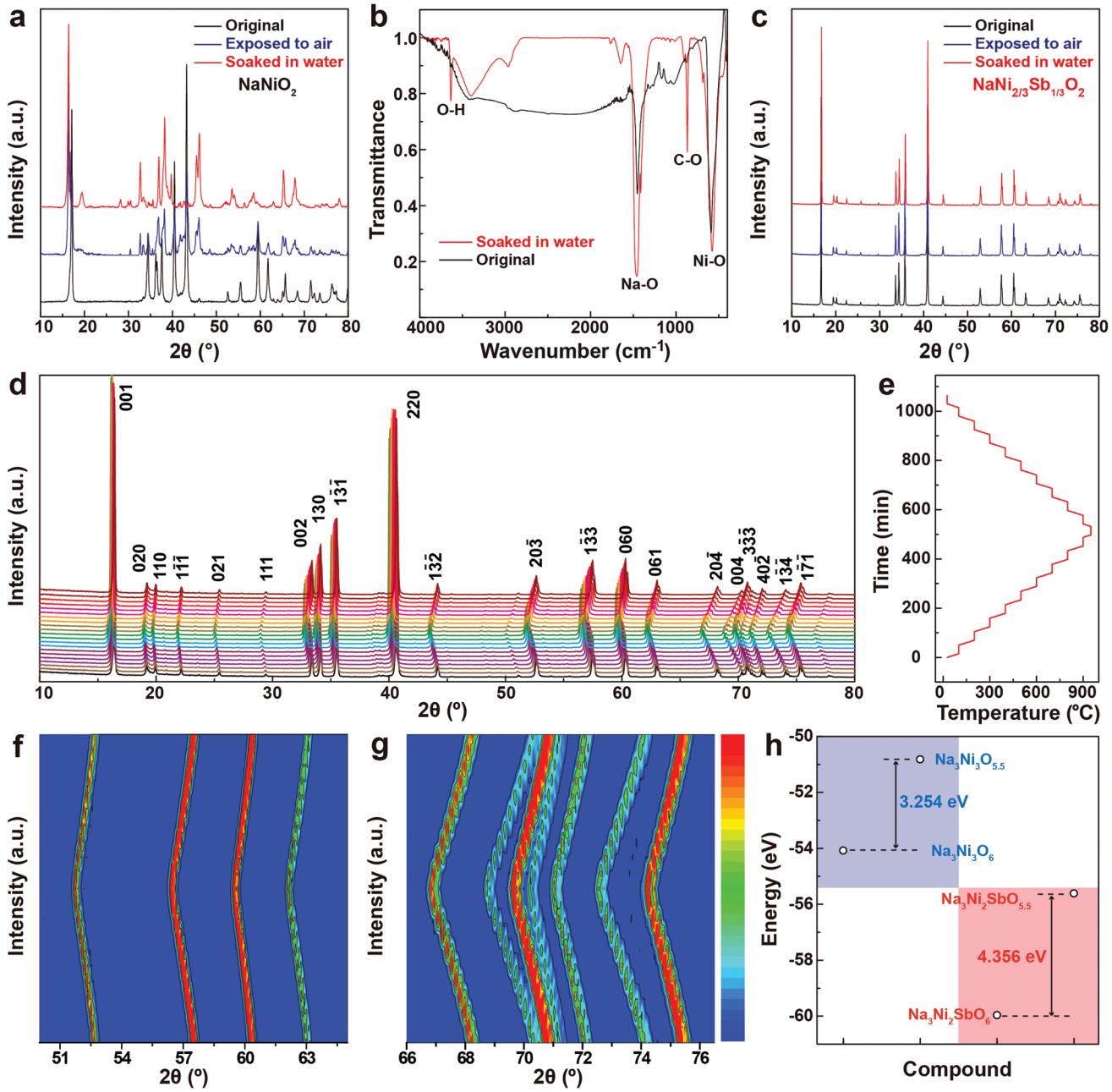

Figure 2. a) XRD patterns of as-synthesized and aged $NaNiO_2$ sample. b) IR spectra of $NaNiO_2$ before and after being soaked in water. c) XRD patterns of as-synthesized and aged $NaNi_{2/3}Sb_{1/3}O_2$ sample. d) In situ XRD patterns of the $NaNi_{2/3}Sb_{1/3}O_2$ material during the thermal treatment process. e) Corresponding heating program chosen for XRD tests. f,g) Contour plot of the evolution of the characteristic diffraction peaks during the thermal treatment process. h) Calculated energy barrier before and after O extraction for $NaNiO_2$ (blue background) and $NaNi_{2/3}Sb_{1/3}O_2$ (red background).

$NaNi_{2/3}Sb_{1/3}O_2$, magnetic measurement indicated that onset of antiferromagnetic takes place at 16 K and the frustration parameter approaches 0.75, much smaller than that of $NaNiO_2$.[32] As illustrated in Figure 3e, the electronic spin difference charge density of $NaNiO_2$ on oxygen atoms shows a shape pointing to a sodium atom and a nickel atom. Whereas, no charge density pointing to two different Ni atoms can be found. In comparison, the spin difference charge density on oxygen atoms exhibits a shape pointing to two neighboring nickel atoms in $NaNi_{2/3}Sb_{1/3}O_2$, manifesting a strong Ni–O–Ni 90° super-exchange interaction,[33] which is indicated by a blue arrow (Figure 3f) and promotes its structural stability.

The electrochemistry of $NaNiO_2$ and $NaNi_{2/3}Sb_{1/3}O_2$ was then incorporated in half Na cells (**Figure 4**a). Various voltage plateaus and steps are obviously observed in the charge/discharge curves of the $NaNiO_2$, indicating several phase transitions of O3–P′3–P″3–O′3–O″3 occurring along with NiO_2 slab gliding.[34] When 1/3 Sb is introduced into the crystal framework, the multiple voltage plateaus are simplified to two main plateaus at 3.26 V (O3–P3 transition) and 3.64 V (P3–O1

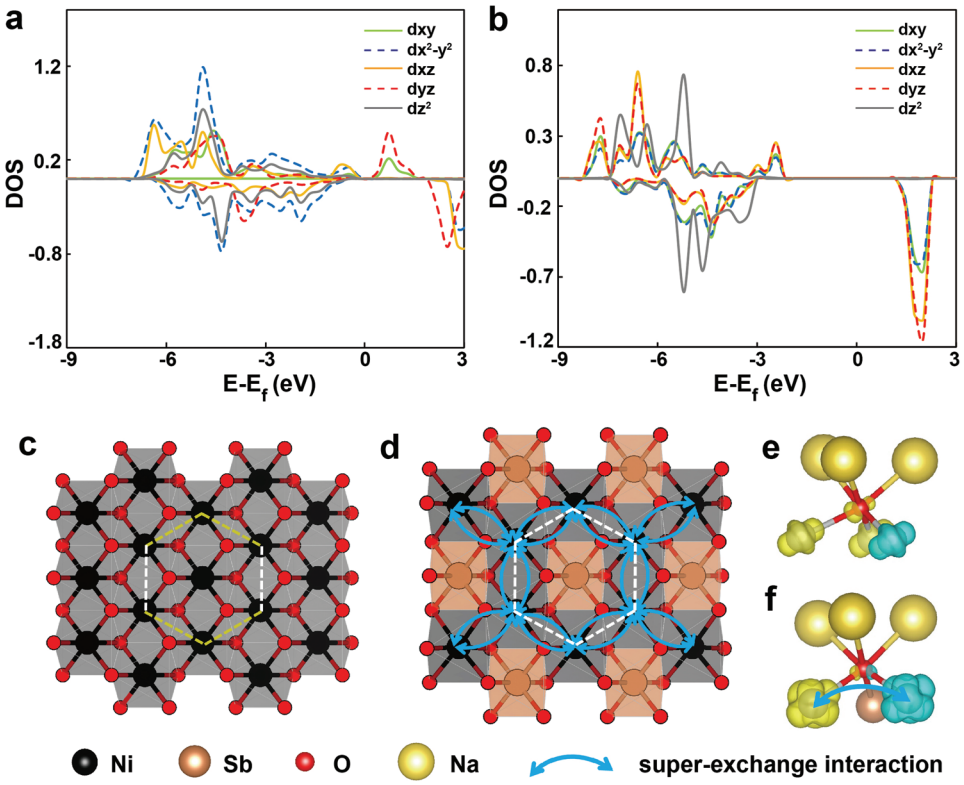

Figure 3. a,b) The partial density of states (pDOS) of $NaNiO_2$ (a) and $NaNi_{2/3}Sb_{1/3}O_2$ (b). c,d) The comparison of bond length of $NaNiO_2$ (c) and $NaNi_{2/3}Sb_{1/3}O_2$ structure (d). e,f) The spin difference charge density of $NaNiO_2$ (e) and $NaNi_{2/3}Sb_{1/3}O_2$ (f).

transition) without affecting the capacity.[35] The calculated voltages of $NaNi_{2/3}Sb_{1/3}O_2$ are consistent with experimental voltage from P3 to O1 upon charge and P3 to O3 during discharge. Notably, slight voltage polarization are observed for O3–P3 and O1–P3 phase transition voltage, which might be caused by the energy loss from a symmetrical electronic structure (O1 or O3) to an asymmetrical electronic structure (P3) as discussed later. Several P3 and O1 structures are chosen to obtain the most energy favorable structure in order to match the experimental voltage. Corresponding convex hull is plotted in Figure 4b and Figure S9 (Supporting Information). Intermediate P3 phase can be finally written as $Na_{1/2}Ni_{2/3}Sb_{1/3}O_2$ due to the lowest energy and the suited calculated voltage. The detailed structural evolution of O3–P3–O1 accompanied by transition metal layers glides is illustrated in Figure 4c. Obviously, from a stepwise voltage profile observed for $NaNiO_2$, unsatisfactory battery performance is achieved as the phase boundary movement for more biphasic regions is required. In contrast, both original and aged $NaNi_{2/3}Sb_{1/3}O_2$ electrodes show an initial charge capacity of 120 mA h g^{-1} with a capacity retention of 82% after 50 cycles owing to the simplified phase transition behavior (Figures S10–S12).

Figure 4d shows the contour maps of experimental operando XRD patterns for the phase stability of $Na_{1-x}Ni_{2/3}Sb_{1/3}O_2$ during initial Na extraction. O3 structure first shows steep structural change into P3 structure then another structural transition from P3 to O1 phase at higher regions. Single phase of P3 and O1 structure can be found at 3.5 and 4.0 V, respectively (Figure S13, Supporting Information). The indirect in-plane honeycomb ordering of $Na_{1-x}Ni_{2/3}Sb_{1/3}O_2$ from powder diffraction data was determined through direct transmission electron microscopy (TEM) studies. Figure 4e–g shows selected area electron patterns (SAED) of monoclinic O3, monoclinic P3 and hexagonal O1 phase. The ordering of the honeycomb layer in three compounds is evident in the *a*–*b* plane. The $R\bar{3}m$ subcell can fully index the major electron diffraction peaks, however, many additional superstructure reflections can only be indexed by an ideal trigonal $P3_112$ superstructure rather than the true $C2/m$ monoclinic superstructure, such as the 100_P and 200_P reflections along the $[001]_P$ direction.[36] The patterns of P3 phase is slightly different from the O3-$NaNi_{2/3}Sb_{1/3}O_2$ and O1-$Na_{1/3}Ni_{2/3}Sb_{1/3}O_2$, in contrast with the change law of orbital degeneracy of O3, P3 and O1 structures as discussed in later sections.

Ex situ hard X-ray absorption study was carried out to study the charge compensation mechanism of $Na_{1-x}Ni_{2/3}Sb_{1/3}O_2$ in the bulk during charge/discharge process. As charge increases from 2.0 to 4.0 V, the shifts of X-ray absorption near-edge structure (XANES) spectra (**Figure 5**a) at Ni K-edge resembles the edge position of reference Ni oxides Ni(II)O and LiNi(III)O_2, suggesting the sequential oxidation of $Ni^{2+} \rightarrow Ni^{3+}$.[37] The intensity of pre-edge peak at Ni K-edge always maintains very weak, indicating that the nickel ions in $Na_{1-x}Ni_{2/3}Sb_{1/3}O_2$ remain in octahedral sites upon Na extraction and insertion. In contrast, no apparent changes are observed for the Sb K-edges (Figure 5b), revealing that the pentavalent antimony ions do not participate in the electrochemical reaction. Corresponding extended X-ray absorption fine structure (EXAFS) spectra at

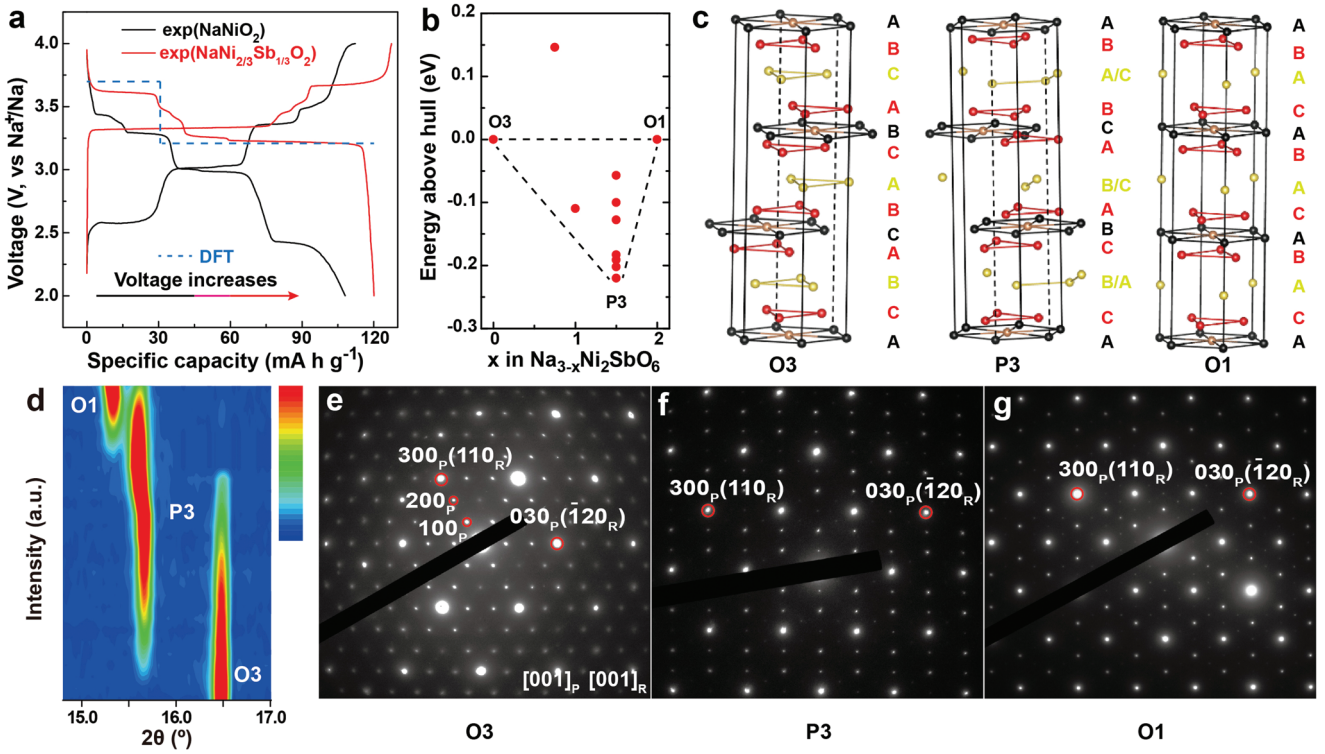

Figure 4. a) Calculated voltage plot (DFT) compared with experimentally obtained charge/discharge profile of $NaNi_{2/3}Sb_{1/3}O_2$. b) Formation energies of O3, P3, and O1 structures for $Na_{3-x}Ni_2SbO_2$ as a function of Na content (x) obtained using ab initio DFT calculations. c) The Ni_6-ring structure evolution of $Na_{1-x}Ni_{2/3}Sb_{1/3}O_2$: red, black, yellow, and brown indicates oxygen, nickel, sodium and antimony, respectively. d) Contour plot of the (001) diffraction peaks of in situ XRD patterns evolution collected during the first charge of the $Na_{1-x}Ni_{2/3}Sb_{1/3}O_2$ cells. e–g) SAED patterns of typical O3, P3, and O1 phase.

the Ni and Sb K-edges (Figure 5c,d) provide the interatomic distance information of $Na_{1-x}Ni_{2/3}Sb_{1/3}O_2$. In the first M–O coordination shell, the Ni K-edge delivers lowered Fourier transform (FT) magnitude and shortened inter atomic distance with the oxidation of Ni^{2+} to Jahn–Teller active Ni^{3+}, while almost no change is observed at the Sb K-edge as charge increases. In the M–M second coordination shells, because three Ni and three Sb atoms surround one Ni atom while every Sb atom is only coordinated by six Ni atoms. There are two kinds of Ni–Ni and Ni–Sb environment and only one Sb–Ni peak in the second coordination shells, further confirming a perfect honeycomb ordering within the MO_2 slabs.

Soft X-ray absorption collected in total fluorescence yield (TFY) and total electron yield (TEY) modes can provide further contrast between bulk and surface regions. Bulk-sensitive TFY and surface sensitive TEY signals of $Na_{1-x}Ni_{2/3}Sb_{1/3}O_2$ at Ni L-edge and O K-edge upon Na (de)intercalation are displayed as solid and dotted lines, respectively. There is a main peak at 852.5 eV with a satellite peak at 854.8 eV at the Ni L-edge TFY spectrum for $NaNi_{2/3}Sb_{1/3}O_2$ (Figure 5e), which is typical of high-spin Ni^{2+}.[38] Upon Na extraction and insertion, the intensity of the satellite peak shows reversible increases (decreases), revealing nickel ions changes reversibly from Ni^{2+} to Ni^{4+} in the electronic state of the $[NiO_6]n^-$ cluster in $Na_{1-x}Ni_{2/3}Sb_{1/3}O_2$. Different from the bulk sensitive TFY results, there is a stable Ni^{2+} layer on the surface of $Na_{1-x}Ni_{2/3}Sb_{1/3}O_2$ by sensitive TEY signals, suggesting O1 phase coexists with Ni^{2+} and Ni^{4+} at the final charged state. Based on $L_3/(L_3+L_2)$ branch ratio of Ni-L edge XAS results (0.77–0.78 for TEY mode, 0.60–0.63 for TFY mode), it can be concluded that the Ni redox couple involves losing (oxidizing) or adding (reducing) electrons in the spin-up e_g orbital.[39] In O K-edge XAS (Figure 5f), the pre-edge feature around 532 eV is related to the O 1s to 2p transition, and its intensity is associated with the density of unoccupied Sb 4d–O 2p and Ni 3d–O 2p hybridized states.[40] When Na is extracted from the lattice, the pre-edge intensity at 529 eV exhibits an increase, which originates the stronger hybridization between the higher-valent transition metal Ni^{4+} and the oxygen 2p. Discharging to 120 mA h g^{-1} restores the pre-edge shape and intensity, indicating reversible Ni oxidation/reduction process.

To better understand the charge compensation mechanism, the magnetic moment of Ni valence is investigated (Figure 5g). Ni ions in O3 phase have a magnetic moment around 1.76 μ_B, referring to divalent Ni^{2+}. In P3-$Na_{1/2}Ni_{2/3}Sb_{1/3}O_2$, three types of magnetic moment exists: half of Ni have a magnetic moment of 1.74 μ_B, a quarter is 1.15 μ_B, and the rest is 0.19 μ_B, corresponding to Ni^{2+}, Ni^{3+} and Ni^{4+}, respectively. Two types of magnetic moment of Ni ions are found in O1-$Na_{1/3}Ni_{2/3}Sb_{1/3}O_2$: half is 1.72 μ_B for Ni^{2+}, and half is 0.19 μ_B for Ni^{4+} (agrees with the sXAS results). The specific atomic/electronic structure symmetry of P3-$Na_{1/2}Ni_{2/3}Sb_{1/3}O_2$ and O1-$Na_{1/3}Ni_{2/3}Sb_{1/3}O_2$ phases are illustrated in Figure S14 (Supporting Information). Based on the radial distribution

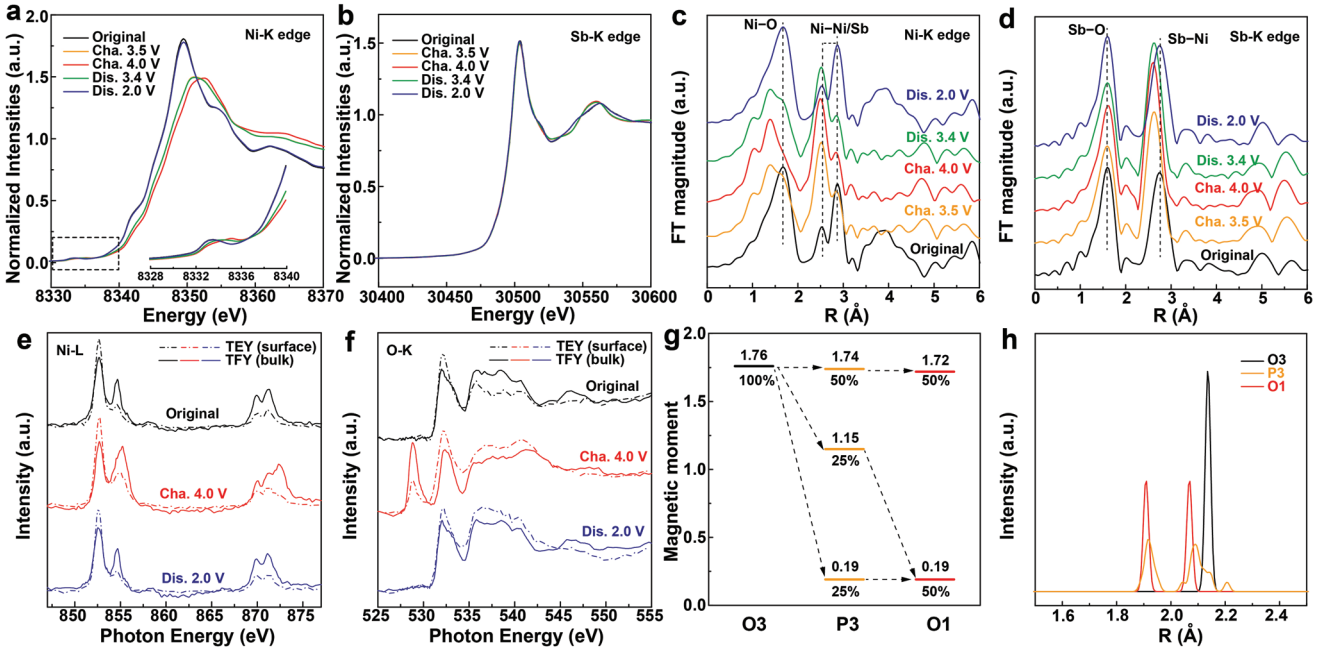

Figure 5. a,b) Ex situ XANES spectra at the Ni K-edge (a) and Sb K-edge (b) of $Na_{1-x}Ni_{2/3}Sb_{1/3}O_2$ electrodes collected at different charge/discharge states. c,d) Corresponding ex situ EXAFS spectra at the Ni K-edge (c) and Sb K-edge (d) of $Na_{1-x}Ni_{2/3}Sb_{1/3}O_2$ electrodes. e) Ni L-edge and f) O K-edge ex situ soft XAS spectra of $Na_{1-x}Ni_{2/3}Sb_{1/3}O_2$ electrodes collected at different charge/discharge states in TEY (dotted line) and TFY (solid line) modes. g) Magnetic moment and h) distribution of Ni—O bond length in O3, P3, and O1 phases.

function (RDF) of neighboring O/Ni atoms (Figure 5h and Figure S15, Supporting Information), the Ni^{2+}—O and Ni^{4+}—O bonds length of P3-$Na_{1/2}Ni_{2/3}Sb_{1/3}O_2$ are located at 2.1 and 1.9 Å, respectively, whereas Ni^{3+} ions have the longest bond length of 2.21 Å and the shortest of 1.91 Å due to their Jahn–Taller effect. As for O1-$Na_{1/3}Ni_{2/3}Sb_{1/3}O_2$, both Ni^{2+} and Ni^{4+} ions under symmetrical environment have equal bonds length free from Jahn–Taller effect. In short, an interesting electronic structural evolution of symmetry–asymmetry–symmetry during O3–P3–O1 phase transformation process is proposed, accompanied by three valence disproportionation of nickel in P3 phase, divalent and tetravalent Ni coexisting in O1 phase.

In summary, a comprehensive study of structural stability, ordering tendencies, and reaction mechanisms has been performed on typical honeycomb ordered $NaNi_{2/3}Sb_{1/3}O_2$ and prototype $NaNiO_2$ materials through both experimental characterizations and calculated strategies. Ordering on the honeycomb in $NaNi_{2/3}Sb_{1/3}O_2$ not only allows this phase to be more stable than square and zigzag structures at the same Na concentrations, but also significantly enhance its whole structural stability in terms of air, thermal and phase stability. Detailed atomic and electronic structure analysis reveals that the dramatically enhanced stability is associated with averaged bonds length and degenerated orbital by the super-exchange interaction of Ni_6-ring structure unit in $NaNi_{2/3}Sb_{1/3}O_2$, which provides a rigid framework upon sodium-ion transport, simultaneously simplifies multiple phase evolution, and critically influences the battery cycle stability of both capacity and voltage. Therefore, reasonable ionic incorporation with very different bond energy and compatible ionic radii in layered materials, such as V^{5+}, Bi^{5+}, Sb^{5+}, As^{5+}, and Te^{6+}, might be a sensible strategy to modulate the ordering of the metal lattice in order to enhance their structural stability (Figure S16, Supporting Information). The present work sheds light on how in-plane ordered superstructure can affect the structural stability and battery performance, which could provide new guidelines for designing highly stable electrode materials.

Supporting Information

Supporting Information is available from the Wiley Online Library or from the author.

Acknowledgements

P.-F.W., M.W., and Y.X. contributed equally to this work. This work was supported by the Basic Science Center Project of the National Natural Science Foundation of China (Grant No. 51788104), the National Natural Science Foundation of China (Grant Nos.51772301 and 21773264), the National Key R&D Program of China (Grant Nos.2016YFA0202500 and 2016YFB0700600), Soft Science Research Project of Guangdong Province (No. 2017B030301013), Shenzhen Science and Technology Research Grant (ZDSYS201707281026184) and the "Transformational Technologies for Clean Energy and Demonstration," Strategic Priority Research Program of the Chinese Academy of Sciences (Grant No.XDA21070300). The authors acknowledge Yang Sun for XRD analysis at ICCAS and the support from the BL14W1 beam-lines of the Shanghai Synchrotron Radiation Facility (SSRF), China. The authors also acknowledge Dr. Wanli Yang for sXAS data collection and procession. This research used resources of the Advanced Light Source, which is a U.S. Department of Energy Office of Science User Facility under contract no. DE-AC02-05CH11231.

Conflict of Interest

The authors declare no conflict of interest.

Keywords

cathode, electrochemistry, Ni_6-ring, sodium-ion batteries, superstructure

Received: June 1, 2019
Revised: July 11, 2019
Published online: September 8, 2019

[1] N. Yabuuchi, K. Kubota, M. Dahbi, S. Komaba, *Chem. Rev.* **2014**, *114*, 11636.
[2] R. Berthelot, D. Carlier, C. Delmas, *Nat. Mater.* **2011**, *10*, 74.
[3] Y. Wang, R. Xiao, Y.-S. Hu, M. Avdeev, L. Chen, *Nat. Commun.* **2015**, *6*, 6954.
[4] M. Lee, J. Hong, J. Lopez, Y. Sun, D. Feng, K. Lim, W. C. Chueh, M. F. Toney, Y. Cui, Z. Bao, *Nat. Energy* **2017**, *2*, 861.
[5] K. Kubota, S. Kumakura, Y. Yoda, K. Kuroki, S. Komaba, *Adv. Energy Mater.* **2018**, *8*, 1703415.
[6] C. Delmas, C. Fouassier, P. hagenmuller, *Physica B+C* **1980**, *99*, 81.
[7] J. Ma, P. Hu, G. Cui, L. Chen, *Chem. Mater.* **2016**, *28*, 3578.
[8] J. Yang, H. Zhang, Q. Zhou, H. Qu, T. Dong, M. Zhang, B. Tang, J. Zhang, G. Cui, *ACS Appl. Mater. Interfaces* **2019**, *11*, 17109.
[9] P.-F. Wang, Y. You, Y.-X. Yin, Y.-G. Guo, *Adv. Energy Mater.* **2018**, *8*, 1701912.
[10] M. H. Han, E. Gonzalo, G. Singh, T. Rojo, *Energy Environ. Sci.* **2015**, *8*, 81.
[11] C. Fang, Y. Huang, W. Zhang, J. Han, Z. Deng, Y. Cao, H. Yang, *Adv. Energy Mater.* **2016**, *6*, 1501727.
[12] R. J. Clément, P. G. Bruce, C. P. Grey, *J. Electrochem. Soc.* **2015**, *162*, A2589.
[13] D. Buchholz, L. G. Chagas, C. Vaalma, L. Wu, S. Passerini, *J. Mater. Chem. A* **2014**, *2*, 13415.
[14] S. Kim, K. W. Nam, S. Lee, W. Cho, J. S. Kim, B. G. Kim, Y. Oshima, J. S. Kim, S. G. Doo, H. Chang, D. Aurbach, J. W. Choi, *Angew. Chem., Int. Ed.* **2015**, *54*, 15094.
[15] H.-R. Yao, P.-F. Wang, Y. Gong, J. Zhang, X. Yu, L. Gu, C. OuYang, Y.-X. Yin, E. Hu, X.-Q. Yang, E. Stavitski, Y.-G. Guo, L.-J. Wan, *J. Am. Chem. Soc.* **2017**, *139*, 8440.
[16] Y. Zhang, R. Zhang, Y. Huang, *Front. Chem.* **2019**, *7*, 335.
[17] S. P. Ong, V. L. Chevrier, G. Hautier, A. Jain, C. Moore, S. Kim, X. Ma, G. Ceder, *Energy Environ. Sci.* **2011**, *4*, 3680.
[18] L. Wang, B. Chen, J. Ma, G. Cui, L. Chen, *Chem. Soc. Rev.* **2018**, *47*, 6505.
[19] D. Chang, H. Huo, K. E. Johnston, M. Ménétrier, L. Monconduit, C. P. Grey, A. Van der Ven, *J. Mater. Chem. A* **2015**, *3*, 18928.
[20] C. Didier, M. Guignard, M. R. Suchomel, D. Carlier, J. Darriet, C. Delmas, *Chem. Mater.* **2016**, *28*, 1462.
[21] J. Vinckevičiūtė, M. D. Radin, A. Van der Ven, *Chem. Mater.* **2016**, *28*, 8640.
[22] Y. Qi, Q. Xu, A. Van der Ven, *J. Electrochem. Soc.* **2012**, *159*, A1838.
[23] W. H. Woodford, Y.-M. Chiang, W. C. Carter, *J. Electrochem. Soc.* **2013**, *160*, A1286.
[24] A. J. Toumar, S. P. Ong, W. D. Richards, S. Dacek, G. Ceder, *Phys. Rev. Appl.* **2015**, *4*, 064002.
[25] W. Schmidt, R. Berthelot, A. W. Sleight, M. A. Subramanian, *J. Solid State Chem.* **2013**, *201*, 178.
[26] X. Lu, Y. Wang, P. Liu, L. Gu, Y. S. Hu, H. Li, G. P. Demopoulos, L. Chen, *Phys. Chem. Chem. Phys.* **2014**, *16*, 21946.
[27] K. Kubota, S. Komaba, *J. Electrochem. Soc.* **2015**, *162*, A2538.
[28] Y. You, A. Dolocan, W. Li, A. Manthiram, *Nano Lett.* **2019**, *19*, 182.
[29] Z. Hu, J. Zheng, C. Xin, G. Teng, Y. Zuo, F. Pan, *J. Phys. Chem. C* **2018**, *122*, 4125.
[30] Y. Xiao, T. Liu, J. Liu, L. He, J. Chen, J. Zhang, P. Luo, H. Lu, R. Wang, W. Zhu, Z. Hu, G. Teng, C. Xin, J. Zheng, T. Liang, F. Wang, Y. Chen, Q. Huang, F. Pan, H. Chen, *Nano Energy* **2018**, *49*, 77.
[31] F. Vernay, K. Penc, P. Fazekas, F. Mila, *Phys. Rev. B* **2004**, *70*, 014428.
[32] E. A. Zvereva, M. I. Stratan, Y. A. Ovchenkov, V. B. Nalbandyan, J. Y. Lin, E. L. Vavilova, M. F. Iakovleva, M. Abdel-Hafiez, A. V. Silhanek, X. J. Chen, A. Stroppa, S. Picozzi, H. O. Jeschke, R. Valentí, A. N. Vasiliev, *Phys. Rev. B* **2015**, *92*, 144401.
[33] J. Zheng, G. Teng, C. Xin, Z. Zhuo, J. Liu, Q. Li, Z. Hu, M. Xu, S. Yan, W. Yang, F. Pan, *J. Phys. Chem. Lett.* **2017**, *8*, 5537.
[34] M. H. Han, E. Gonzalo, M. Casas-Cabanas, T. Rojo, *J. Power Sources* **2014**, *258*, 266.
[35] D. Yuan, X. Liang, L. Wu, Y. Cao, X. Ai, J. Feng, H. Yang, *Adv. Mater.* **2014**, *26*, 6301.
[36] J. Ma, S.-H. Bo, L. Wu, Y. Zhu, C. P. Grey, P. G. Khalifah, *Chem. Mater.* **2015**, *27*, 2387.
[37] X. Yu, Y. Lyu, L. Gu, H. Wu, S.-M. Bak, Y. Zhou, K. Amine, S. N. Ehrlich, H. Li, K.-W. Nam, X.-Q. Yang, *Adv. Energy Mater.* **2014**, *4*, 1300950.
[38] E. Hu, X. Yu, R. Lin, X. Bi, J. Lu, S. Bak, K.-W. Nam, H. L. Xin, C. Jaye, D. A. Fischer, K. Amine, X.-Q. Yang, *Nat. Energy* **2018**, *3*, 690.
[39] B. T. Thole, G. van der Laan, *Phys. Rev. B* **1988**, *38*, 3158.
[40] F. M. F. de Groot, M. Grioni, J. C. Fuggle, J. Ghijsen, G. A. Sawatzky, H. Petersen, *Phys. Rev. B* **1989**, *40*, 5715.